Orientation effects on near-field radiative heat transfer between complex-shaped dielectric particles

Cite as: Appl. Phys. Lett. **121**, 182206 (2022); https://doi.org/10.1063/5.0116828 Submitted: 29 July 2022 • Accepted: 14 October 2022 • Published Online: 03 November 2022

D Lindsay P. Walter and D Mathieu Francoeur











Orientation effects on near-field radiative heat transfer between complex-shaped dielectric particles

Cite as: Appl. Phys. Lett. **121**, 182206 (2022); doi: 10.1063/5.0116828 Submitted: 29 July 2022 · Accepted: 14 October 2022 · Published Online: 3 November 2022







Lindsay P. Walter 🕞 and Mathieu Francoeur a 🕞

AFFILIATIONS

Radiative Energy Transfer Lab, Department of Mechanical Engineering, University of Utah, Salt Lake City, Utah 84112, USA

Note: This paper is part of the APL Special Collection on Thermal Radiation at the Nanoscale and Applications.

a) Author to whom correspondence should be addressed: mfrancoeur@mech.utah.edu

ABSTRACT

The effect of orientation on near-field radiative heat transfer between two complex-shaped superellipsoid particles of SiO_2 is presented. The particles under study are 50 nm in radius and of variable concavity. Orientation is characterized by the degree of rotational symmetry in the two-particle systems, and the radiative conductance is calculated using the discrete system Green's function approach to account for all electromagnetic interactions. The results reveal that the total conductance in some orientations can be up to twice that of other orientations when particles are at a center-of-mass separation distance of 110 nm. Orientation effects are not significantly correlated with system rotational symmetries but are strongly correlated with the minimum vacuum gap distance between particles. As such, orientation effects on near-field radiative heat transfer are a consequence of particle topology, with more extreme topologies leading to a continuation of orientation effects at larger particle center-of-mass separation distances. The concave superellipsoid particles display significant orientation effects up to a center-of-mass separation distance approximately equal to 3.9 times the particle radius, while the convex superellipsoid particles display significant orientation effects up to a center-of-mass separation distance approximately equal to 3.2 times the particle radius. In contrast to previous anisotropic, spheroidal dipole studies, these results of complex-shaped superellipsoid particles suggest that orientation effects become negligible when heat transfer is a volumetric process for all orientations. This work is essential for understanding radiative transport between particles that have non-regular geometries or that may have geometrical defects or abnormalities.

Published under an exclusive license by AIP Publishing. https://doi.org/10.1063/5.0116828

Micro/nanoparticles are gaining increasing interest for their potential to modulate radiative thermal transport. ^{1–9} In the near-field regime in which interparticle distances are less than the characteristic thermal wavelength defined by Wien's law, radiative transport between micro/nanoparticles is often dominated by shape-dependent surface polaritons and localized surface modes, ^{10–12} opening the possibility for tuning the spectrum of heat transfer and, thus, spectral radiative properties. ^{13,14} Spectral tuning of radiative transfer between micro/nanoparticles finds applications in a wide range of fields, from thermophotovoltaics ^{15–17} to radiative cooling, ^{18,19} metamaterial design, ²⁰ and thermal circuitry. ^{2,21}

Prior research suggests that near-field radiative heat transfer (NFRHT) between anisotropic particles may be tuned by varying the particle orientation. ^{22–26} For example, researchers have studied NFRHT between SiC nanoparticles modeled as prolate and oblate

spheroidal dipoles and found that the heat flux 22,23 and the time evolution of temperature 24 may be modulated by varying the orientation of particles. While some orientations result in minimal heat flux, other orientations result in heat flux values over two orders of magnitude greater than that of spherical dipoles of equivalent volume and center-of-mass separation distance. This large range in heat flux has been attributed to the anisotropic polarizabilities of prolate/oblate spheroidal dipoles, and these results have led to the conclusion that anisotropic nanoparticles may be applied as a sort of thermal switch. In dipole models such as these, Refs. 22-24 and 26, the simplifying approximations require that the center-of-mass separation distance d_c be greater than the particle characteristic length L_{ch} . However, the numerical value of separation distances used in Ref. 22 was not reported, while the dipole approximation was applied to closely spaced particles that did not satisfy the required condition $d_c \gg L_{ch}$ in Ref. 23.

Consequently, it is unclear whether these findings relating the particle orientation to large differences in heat flux represent physical systems. Even when dipole approximations are applied within their regime of validity, these approximations are still quite restrictive and cannot capture the full near-field electromagnetic interactions required for design of real-world particle devices, such as Mie resonance-based metamaterials ^{28–30} and packed particle beds. ¹ Except for a few studies involving two gold cylinders ^{31,32} and two graphene dimers, ²⁵ the impact of orientation on NFRHT between particles beyond the dipole approximation has not been systematically analyzed.

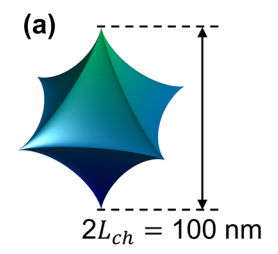
In this Letter, we study the effect of orientation on NFRHT between two complex-shaped dielectric particles made of SiO₂, a material supporting surface phonon-polaritons (SPhPs) in the infrared. The particles are embedded in vacuum. NFRHT between these particles is modeled via the discrete system Green's function (DSGF) method,³³ which is a numerically exact volume integral approach based on fluctuational electrodynamics.³⁴ In the DSGF method, all electromagnetic interactions are defined by computing a complete system Green's function. As such, the particle models presented here include multiple reflections and all higher order poles, thus enabling NFRHT predictions for vacuum gap distances down to the limit of applicability of fluctuational electrodynamics (~10 nm, Refs. 35-37) regardless of the particle characteristic length. Specifically, in order to determine the underlying physics driving orientation effects on NFRHT, we analyze the degree to which rotational symmetries of two-particle systems may be correlated with the radiative conductance. This work fills the knowledge gaps left from previous studies on particle orientation and is essential for providing the fundamental insight necessary to tune thermal radiation with particles both in the near and far field.

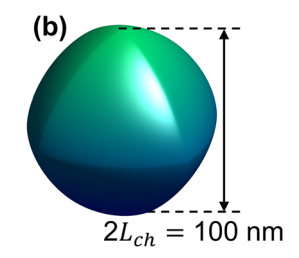
The complex-shaped particles studied in this work are modeled as superellipsoids of variable concavity. Superellipsoid particles were chosen because of their many-fold enhancement in photo/electrocatalytic behavior as compared with cubic nanoparticles, ^{38,39} because they can easily be packed into a variety of superstructure formations, ^{40,41} and because the rotational symmetries in two-particle systems may be systematically controlled. We model two different superellipsoid particle geometries: concave superellipsoids and convex superellipsoids [Figs. 1(a) and 1(b)]. Superellipsoid surfaces are defined as

$$\left(\frac{x}{R_x}\right)^{p_x} + \left(\frac{y}{R_y}\right)^{p_y} + \left(\frac{z}{R_z}\right)^{p_z} = 1,\tag{1}$$

where x, y, and z are Cartesian coordinates; p_x , p_y , and p_z specify the curvature; and R_x , R_y , and R_z are the axial radii. Here, $R_x = R_y = R_z = R = 50$ nm and $p_x = p_y = p_z = p$, where p = 0.75 defines concave superellipsoids and p = 1.5 defines convex superellipsoids. The characteristic length of each particle is taken as the largest radius and is the same for both superellipsoid shapes, $L_{ch} = R = 50$ nm.

The center-of-mass separation distances modeled here span $110 \, \mathrm{nm} \leq d_c \leq 300 \, \mathrm{nm}$, a range from the dipole limit down to distances at which vacuum gaps d are only a fraction of the characteristic length of the particles. The DSGF method is applicable in this entire range of separation distances as long as adequately refined discretization is used. (More details on particle discretization are provided in the supplementary material, Table SI and Fig. S1.) Six different particle orientations were chosen for variable degree of rotational symmetries





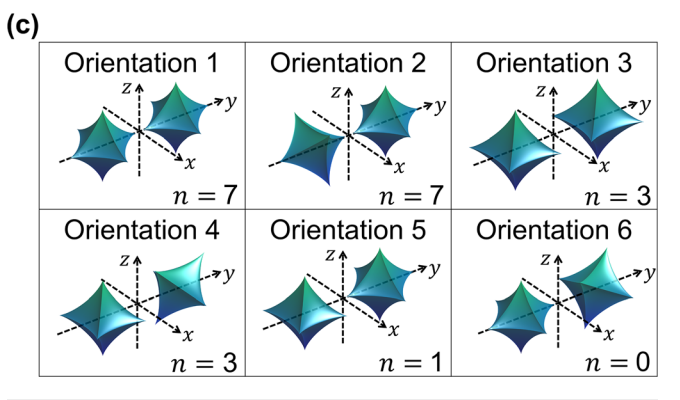


FIG. 1. Superellipsoid SiO₂ particles of variable shape and same characteristic length, $L_{ch} = 50$ nm: (a) concave superellipsoid (p = 0.75) and (b) convex superellipsoid (p = 1.5). (c) Two-particle systems of variable degree of rotational symmetry n as calculated by the algorithm in Ref. 42. Particles are modeled using the software in Ref. 43.

of the two-particle system, where orientations 1 and 2 have the highest degree of rotational symmetry and orientation 6 has the lowest degree of rotational symmetry [Fig. 1(c)]. The degree of rotational symmetry n is defined as the number of isometries around all axes of symmetry in each two-particle system. Rotation angles and axes of symmetry for each isometry were found using the algorithm in Ref. 42 (see the supplementary material, Sec. S2).

Since one of the aims of this work is to determine whether orientation effects on NFRHT may be correlated with the degree of rotational symmetry in a two-particle system, the total and spectral conductance are chosen as the parameters for characterizing NFRHT. All conductance values are calculated at room temperature, $T=300\,\mathrm{K}$. The total conductance $G_{t,AB}(T)$ and spectral conductance $G_{AB}(\omega,T)$ between particles A and B are defined as

$$G_{t,AB}(T) = \frac{1}{2\pi} \int_{0}^{\infty} G_{AB}(\omega, T) d\omega$$

$$= \frac{1}{2\pi} \int_{0}^{\infty} \left[\frac{\partial \Theta(\omega, T')}{\partial T} \right]_{T'=T} \mathcal{T}_{AB}(\omega) d\omega, \tag{2}$$

where $\Theta(\omega,T)$ is the energy of a harmonic oscillator defined as $\Theta(\omega,T)=\hbar\omega\left[\exp\left(\frac{\hbar\omega}{k_BT}\right)-1\right]^{-1}$, with \hbar denoting Planck's constant, ω the angular frequency, k_B the Boltzmann constant, and T the temperature. $\mathcal{T}_{AB}(\omega)$ is the transmission coefficient between particles A and B defined as

$$\mathcal{T}_{AB}(\omega) = \sum_{i \in V_A} \sum_{j \in V_B} 4k_0^4 \Delta V_i \Delta V_j \operatorname{Im}[\varepsilon(\mathbf{r}_i, \omega)] \operatorname{Im}[\varepsilon(\mathbf{r}_j, \omega)]$$
$$\operatorname{Tr}\left[\stackrel{=}{\mathbf{G}} (\mathbf{r}_i, \mathbf{r}_j, \omega) \stackrel{=}{\mathbf{G}}^{\dagger} (\mathbf{r}_i, \mathbf{r}_j, \omega) \right]. \tag{3}$$

In the above equation, i and j are indices for each cubic subvolume of the discretized lattice used in the DSGF method, sums are taken over the entire volume of particles A and B, k_0 is the vacuum wavevector defined as $k_0 = \omega \sqrt{\mu_0 \varepsilon_0}$, with μ_0 and ε_0 being the vacuum permeability and permittivity, respectively, ΔV_i is the volume of the i th subvolume used in the particle discretization, ε is the dielectric function, \mathbf{r}_i and \mathbf{r}_j are the locations of the center points of the i th and j th subvolumes, respectively, $\mathbf{\bar{G}}\left(\mathbf{r}_i,\mathbf{r}_j,\omega\right)$ is the 3×3 DSGF tensor describing the interaction between subvolumes located at \mathbf{r}_i and \mathbf{r}_j , and \dagger denotes the conjugate transpose. The dielectric function of SiO₂ is calculated using a multiple-oscillator Lorentz model with parameters taken from Ref. 44

$$\varepsilon(\omega) = \varepsilon_{\infty} + \sum_{n=1}^{3} \left[\frac{S_n}{1 - \left(\frac{\omega}{\omega_{0,n}}\right)^2 - i\Gamma_n\left(\frac{\omega}{\omega_{0,n}}\right)} \right],\tag{4}$$

where ε_{∞} is the high-frequency permittivity limit, S_n is the absorption strength, $\omega_{0,n}$ is the natural frequency, and Γ_n is the damping constant.

The average runtime for a typical simulation of two particles at one orientation with 17 002 total subvolumes was 44 core hours per frequency running on an AMD Rome processor with 64 cores and 256 GB of RAM. This runtime translates to 4930 total core hours, or a total of 3.2 days of real time, to calculate the integrated total conductance over 111 frequencies at one orientation and a single separation distance.

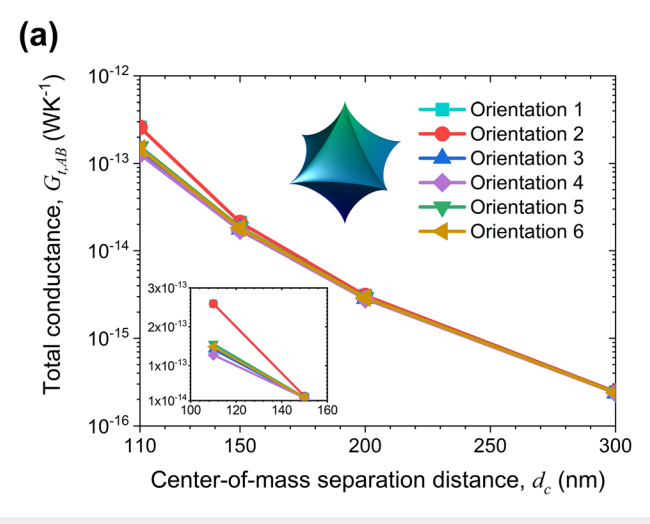
The total conductance plotted as a function of the center-of-mass separation distance reveals that there is no strong correlation between the degree of rotational symmetry in these two-particle systems and NFRHT trends [Figs. 2(a) and 2(b)]. While the particle orientation has

a clear impact on the total conductance when particles are at the closest center-of-mass separation distance $d_c=110\,\mathrm{nm}$, this effect is not significantly related to the degree of system rotational symmetries. As can be seen in Figs. 2(a) and 2(b), the high-symmetry systems (orientations 1 and 2) display the largest total conductance values at the closest center-of-mass separation distance $d_c=110\,\mathrm{nm}$, but this relation does not hold for decreasing rotational symmetries. For example, orientation 6 has the lowest degree of rotational symmetry, but the total conductance of this orientation is only the third smallest out of all the orientations at the closest separation distance $d_c=110\,\mathrm{nm}$ [see insets in Figs. 2(a) and 2(b)].

To quantify the extent to which the orientation influences the total conductance at each center-of-mass separation distance, we consider the normalized range of the total conductance [Fig. 3(a)]. By considering the normalized, rather than the unnormalized, range of the total conductance, the orientation-dependent spread in conductance values can be directly compared across all particle separation distances. The normalized range \overline{R} of a general parameter X at a given center-of-mass separation distance d_c is defined as the range of that parameter over all orientations divided by the mean of that parameter over all orientations

$$\overline{R}[X(d_c)] = \frac{\text{range}\left[X_{orient,1}(d_c), X_{orient,2}(d_c), \dots, X_{orient,N}(d_c)\right]}{\text{mean}\left[X_{orient,1}(d_c), X_{orient,2}(d_c), \dots, X_{orient,N}(d_c)\right]}, (5)$$

where N=6 is the sample size of orientations. More accurate normalized range values could be obtained from a larger sample size of orientations. However, even for the sample of six orientations considered here, we expect the general trends observed in the normalized range of the total conductance to hold for larger orientation sample sizes. At $d_c=110\,\mathrm{nm}$, the normalized range of the total conductance is 0.72 and 0.54 for concave and convex superellipsoid particles, respectively. These ranges correspond to significant orientation effects on NFRHT. The total conductance of concave superellipsoid particles in orientation 1 (i.e., the orientation with the largest total conductance, $G_{t,AB}=2.60\times10^{-13}\,\mathrm{W/K}$) is about two times higher than that of these



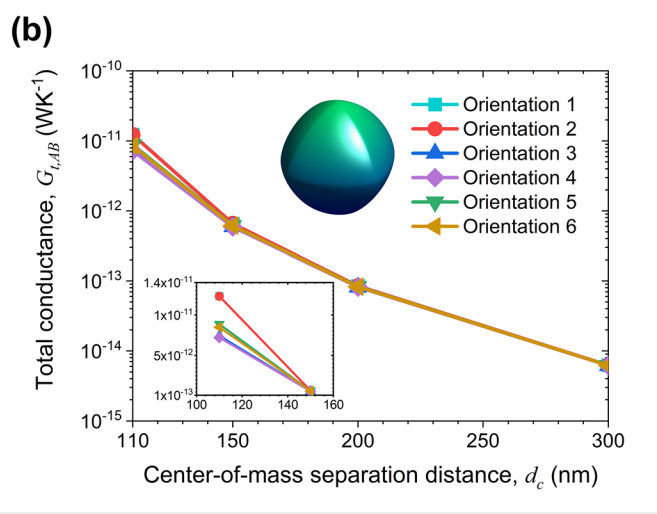
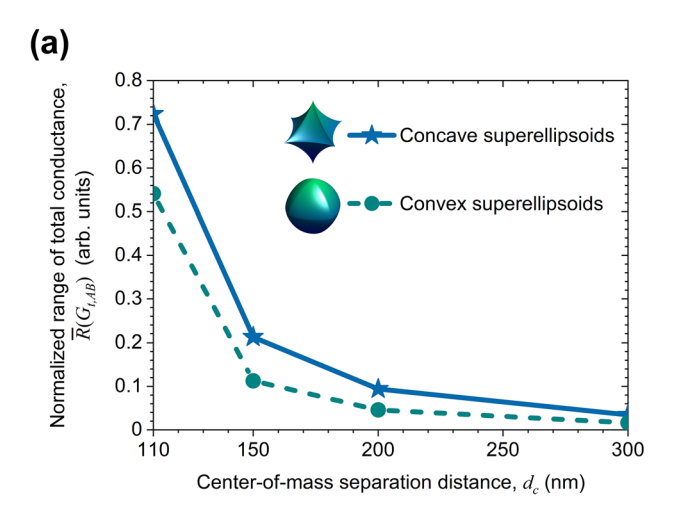


FIG. 2. Total conductance for (a) concave superellipsoid and (b) convex superellipsoid SiO₂ particles vs center-of-mass separation distance for all six orientations. Conductance is calculated at temperature $T = 300 \, \text{K}$. (Insets) Total conductance for the two closest center-of-mass separation distances, $d_c = 110 \, \text{and} \, d_c = 150 \, \text{nm}$ (linear scale).



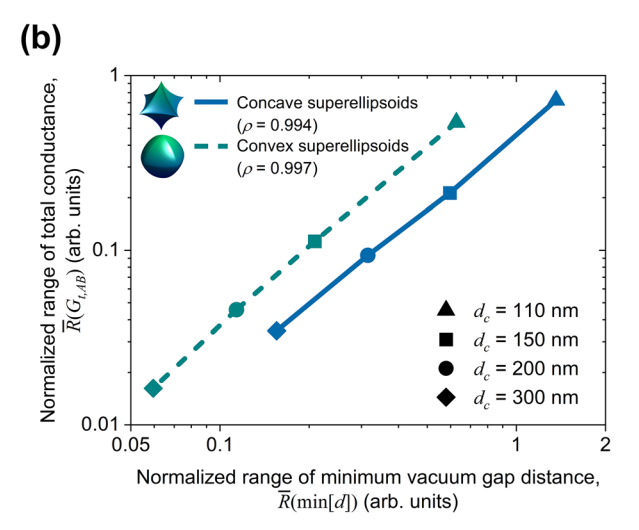


FIG. 3. (a) Normalized range of the total conductance (calculated at temperature $T=300\,\mathrm{K}$) as a function of the center-of-mass separation distance for both particle shapes. (b) Correlation between the normalized range of total conductance and the normalized range of the minimum vacuum gap for both particle shapes evaluated at each center-of-mass separation distance. ρ is the Spearman correlation coefficient calculated as $\rho = \frac{\sum_{i=1}^{N} (x_i - \mu_X)(Y_i - \mu_Y)}{\sqrt{\sum_{i=1}^{N} (x_i - \mu_X)(Y_i - \mu_Y)}}$, where N=6 for the six different particle orientations,

X and Y are the two parameters under analysis (here, the total conductance $G_{t,AB}$ and the minimum vacuum gap distance min[d]), and μ_X is the mean of parameter X. Values of ρ close to unity signify a statistically significant correlation between parameters.

particles in orientation 4 (i.e., the orientation with the smallest total conductance, $G_{t,AB}=1.28\times 10^{-13}$ W/K). This difference is 1.7 times for convex superellipsoid particles in orientation 1 vs orientation 4. From the normalized range of the total conductance $\overline{R}(G_{t,AB})$, we can define two regimes of NFRHT, one in which orientation effects are significant with $\overline{R}(G_{t,AB}) \geq 0.1$ and one in which orientation effects are considered negligible with $\overline{R}(G_{t,AB}) < 0.1$. The center-of-mass separation distance at which this transition occurs varies with particle shape [Fig. 3(a)]. Interpolating between points, the transition occurs for concave superellipsoid particles at $d_c \approx 197$ nm and for convex superellipsoid particles at $d_c \approx 159$ nm. Orientation effects remain significant for concave superellipsoid particles at farther center-of-mass separation distances than for convex superellipsoid particles.

To identify the underlying factors for this difference in transition distances and to determine what exactly is driving orientation effects in the total conductance, we analyzed a variety of geometric parameters. From this analysis, only one parameter displayed similar trends as the total conductance data, namely, the minimum vacuum gap distance d between particles (see the supplementary material for minimum vacuum gap distance data, Fig. S3). Comparing the normalized range of the total conductance and the normalized range of the minimum vacuum gap at each center-of-mass separation distance, we see that these two parameters are highly correlated [Fig. 3(b) and the supplementary material, Figs. S4(a)-S4(b)]. The Spearman correlation coefficient of these two normalized ranges is significant with values of $\rho=0.994$ for the concave superellipsoid particles and $\rho=0.997$ for the convex superellipsoid particles. This similarity in trends between the minimum vacuum gap distance and the total conductance makes intuitive sense, because heat transfer between SiO₂ particles in the near field is dominated by exponentially decaying SPhPs. 45 At the closest center-of-mass separation distance $d_c = 110$ nm, slight changes in the minimum vacuum gap distance with a change in the particle orientation result in large differences in the electromagnetic fields at interfacing surfaces and, therefore, in large differences in the total conductance. Confinement of heat transfer to the closest interfacing surfaces for particles at $d_c=110\,\mathrm{nm}$ is visualized by the spatial distribution of heat dissipation over the volume of each particle (see Fig. 4 for concave superellipsoid particles). At $d_c=110\,\mathrm{nm}$, NFRHT is predominantly a surface, rather than a volumetric, phenomenon, and, consequently, particle orientation matters.

To see more clearly the effect of particle orientation on SPhP resonances, we analyze the spectral conductance of particles and compare

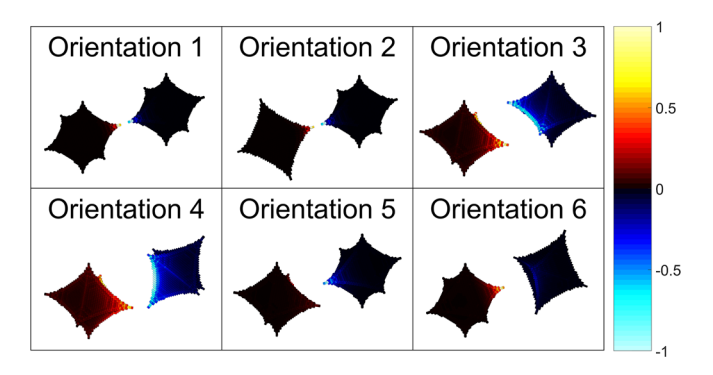


FIG. 4. Spatial distribution of heat dissipation for concave superellipsoid particles of variable orientation at center-of-mass separation distance $d_c=110\,\mathrm{nm}$. The hot particle is at temperature $T=300\,\mathrm{K}$, and the cold particle is at $T=0\,\mathrm{K}$. Heat map colors are normalized by the highest heat dissipation value in each two-particle system, where positive values represent heating and negative values represent cooling. Units are arbitrary.

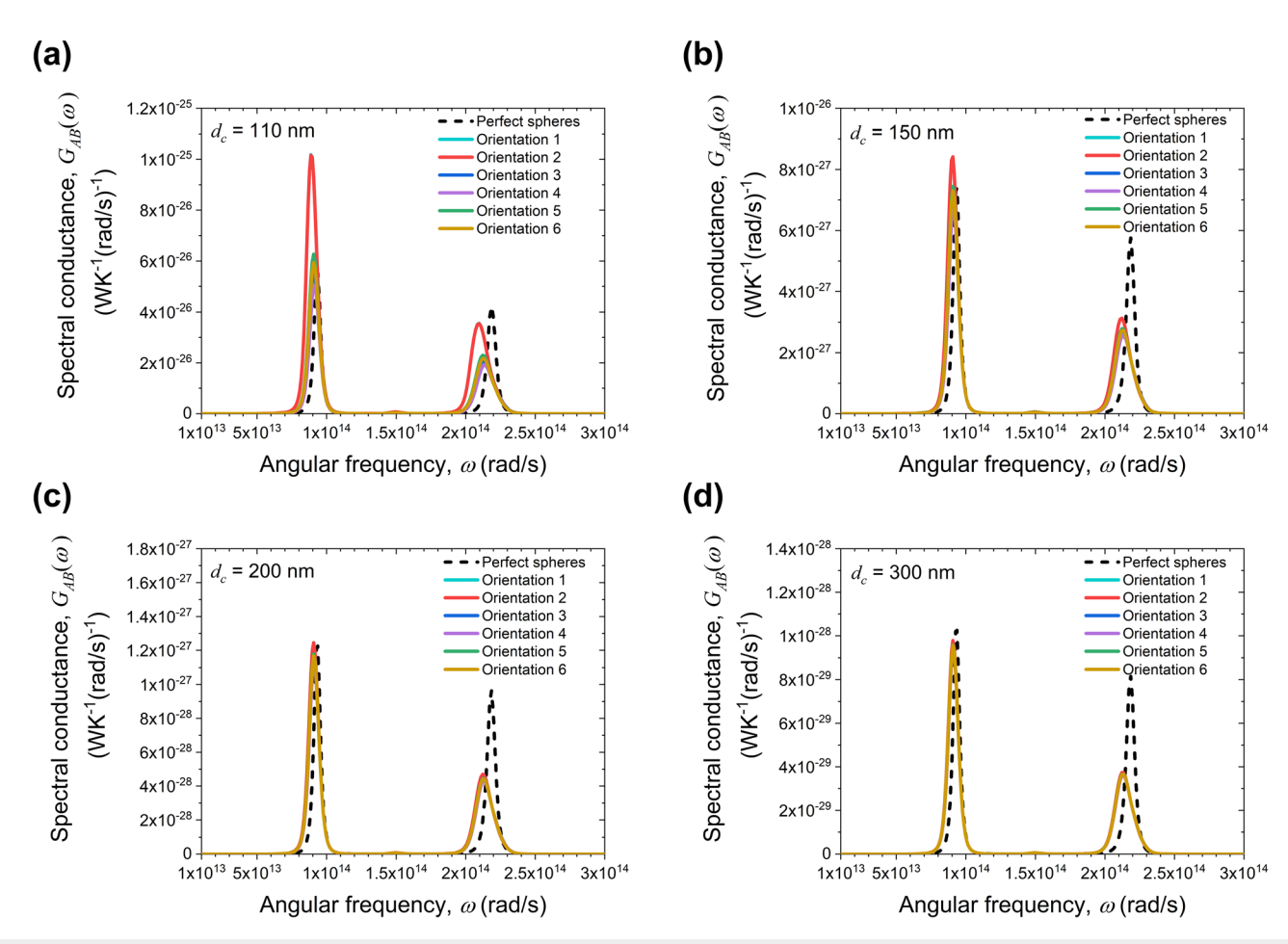


FIG. 5. Spectral conductance at temperature $T=300\,\mathrm{K}$ of concave superellipsoid $\mathrm{SiO_2}$ particles at center-of-mass separation distances (a) $d_c=110$, (b) $d_c=150$, (c) $d_c=200$, and (d) $d_c=300\,\mathrm{nm}$. The spectra of perfect spheres of equivalent volume and center-of-mass separation distance are calculated analytically using the method outlined in Ref. 44.

the spectra against that of a perfect sphere of the same volume and center-of-mass separation distance [see Figs. 5(a)-5(d) for concave superellipsoid particles and the supplementary material for convex superellipsoid particles, Figs. S5(a)-S5(d)]. As shown in the literature on non-spherical particles of regular geometries 10,22,31,46 and in our previous work on irregularly shaped particles,³³ the conductance spectra of non-spherical particles deviate from that of perfect spheres at all center-of-mass separation distances within the near-field regime. Spectral deviation for non-spherical particles is again seen here for superellipsoid particles of all shapes, particularly as it relates to shifts in SPhP resonances. At the closest center-of-mass separation distance $d_c = 110$ nm, the spectral conductance of particles is a function of the particle orientation, especially near SPhP resonances [Fig. 5(a) and the supplementary material, Fig. S5(a)]. This is expected from the previous total conductance results. At the largest center-of-mass separation distance $d_c = 300$ nm, the conductance spectra of different particle orientations converge to a single line, illustrating that NFRHT has become a volumetric process and orientation effects are negligible [Fig. 5(d) and the supplementary material, Fig. S5(d)].

The dipole approximation in NFRHT is typically deemed valid when $d_c \gtrsim 3L_{ch}$. When defining the regimes in which the particle orientation is and is not significant to NFRHT, however, this relation between the particle characteristic length and separation distance is insufficient because it does not account for the geometric shape and spread of particles. These factors are critical in determining precisely when orientation effects should and should not be considered. Using the aforementioned tolerance of 0.1 in the normalized range of the total conductance, orientation effects are considered negligible when $d_c \gtrsim 3.9 L_{ch}$ for concave superellipsoid particles and $d_c \gtrsim 3.2 L_{ch}$ for convex superellipsoid particles. In these relations, the multiplicative factor relating the center-of-mass separation distance d_c and the particle characteristic length L_{ch} is different for each particle shape. The relation may be written in the form of $d_c \ge CL_{ch}$, where C is the shapedependent multiplicative factor. Larger multiplicative factors C reflect a greater spread in the topology of particles that leads to a greater range in vacuum gaps in two-particle systems of variable orientation. For example, we expect the factor C to be larger than that of the superellipsoids shown here when the particles under study have high geometric

anisotropy, such as long wires or flat disks. This prediction is consistent with NFRHT trends seen in clusters of nanoparticles of variable spread and orientation. ^{48,49} Therefore, we recommend that particle shape, especially the degree of topological variation, be taken into account when deciding whether full-scale simulations or simplified approximations are appropriate for modeling NFRHT in a given system of particles.

In conclusion, we have shown that the degree of rotational symmetries in systems of two SiO₂ superellipsoid particles does not appear to be significantly correlated with NFRHT trends. Instead, orientation effects on NFRHT between particles are strongly correlated $(\rho \approx 0.99)$ with the minimum vacuum gap separation distance, and, thereby, a function of the particle topology. This result relating orientation effects on NFRHT to the minimum vacuum gap between particles and particle shape has important consequences in engineering micro/nanoparticle systems for radiative thermal management. Given a group of particles that may contain defects or irregularities, one may approximate when particle orientation effects will and will not be significant for NFRHT by analyzing a representative sample of geometric parameters. Additionally, this work suggests that orientation effects on NFRHT between complex-shaped particles become negligible once particles are in the volumetric regime of NFRHT, a result that differs from previous dipole approximation models.^{22–24} A useful direction for future work is the analysis of orientation effects on NFRHT between particles of other shapes. Such analysis would aid in determining more general, predictive regimes maps of NFRHT so that appropriate modeling techniques may be employed for a given system of particles.

See the supplementary material for the SiO₂ superellipsoid particle discretizations, rotational symmetries in the two-particle systems, comparison of the minimum vacuum gap distance between two superellipsoid SiO₂ particles for all orientations and center-of-mass separation distances, comparison of trends for the normalized range of the total conductance and the normalized range of the minimum vacuum gap distance for two superellipsoid SiO₂ particles, and the spectral conductance between two convex superellipsoid SiO₂ particles.

This work was supported by the National Science Foundation (Grant No. CBET-1952210). L.P.W. acknowledges that this material is based upon work supported by the National Science Foundation Graduate Research Fellowship under Grant No. DGE-1747505. Any opinions, findings, and conclusions or recommendations expressed in this material are those of the authors and do not necessarily reflect the views of the National Science Foundation. The support and resources from the Center for High Performance Computing at the University of Utah are gratefully acknowledged.

AUTHOR DECLARATIONS Conflict of Interest

The authors have no conflicts to disclose.

Author Contributions

Lindsay P. Walter: Conceptualization (equal); Data curation (equal); Formal analysis (equal); Investigation (equal); Methodology (equal); Writing – original draft (equal); Writing – review & editing (equal). **Mathieu Francoeur:** Conceptualization (supporting); Formal analysis

(equal); Funding acquisition (lead); Investigation (supporting); Supervision (lead); Writing – review & editing (supporting).

DATA AVAILABILITY

The data and code that support the findings of this study are available from the corresponding author upon reasonable request.

REFERENCES

- ¹E. Tervo, M. Francoeur, B. Cola, and Z. Zhang, Phys. Rev. B 100, 205422 (2019).
- ²C. Kathmann, M. Reina, R. Messina, P. Ben-Abdallah, and S.-A. Biehs, Sci. Rep. 10, 3596 (2020).
- ³E. Tervo, B. A. Cola, and Z. Zhang, in *Annual Review Heat Transfer* (Begell House, Inc., 2020), pp. 131–166.
- ⁴S. A. Biehs, R. Messina, P. S. Venkataram, A. W. Rodriguez, J. C. Cuevas, and P. Ben-Abdallah, Rev. Mod. Phys. **93**, 25009 (2021).
- ⁵A. Ott, Y. Hu, X. H. Wu, and S.-A. Biehs, Phys. Rev. Appl. 15, 064073 (2021).
- ⁶J.-L. Fang, L. Qu, and H.-L. Yi, Phys. Rev. Appl. 17, 034040 (2022).
- 75. G. Castillo-López, A. Márquez, and R. Esquivel-Sirvent, Phys. Rev. B 105, 155404 (2022).
- ⁸M. Luo, J. Zhao, L. Liu, and M. Antezza, Phys. Rev. B 105, 235431 (2022).
- ⁹Y. Sun, Y. Hu, K. Shi, J. Zhang, D. Feng, and X. Wu, arXiv:2205.12537 (2022).
- ¹⁰O. R. Choubdar and M. Nikbakht, J. Appl. Phys. 120, 144303 (2016).
- ¹¹J. Ordonez-Miranda, L. Tranchant, K. Joulain, Y. Ezzahri, J. Drevillon, and S. Volz, Phys. Rev. B 93, 035428 (2016).
- ¹²P. S. Venkataram, J. Hermann, A. Tkatchenko, and A. W. Rodriguez, Phys. Rev. Lett. **121**, 45901 (2018).
- ¹³S. Shin and R. Chen, Phys. Rev. Appl. **14**, 064013 (2020).
- ¹⁴G. Lu, C. R. Gubbin, J. R. Nolen, T. Folland, M. J. Tadjer, S. D. Liberato, and J. D. Caldwell, Nano Lett. 21, 1831–1838 (2021).
- ¹⁵A. Ghanekar, L. Lin, and Y. Zheng, Opt. Express 24, A868–A877 (2016).
- ¹⁶C. Meng, Y. Liu, Z. Xu, H. Wang, and X. Tang, Energy **239**, 121884 (2022).
- ¹⁷Y. Zhang, Q. Cai, S. Cao, Q. Zhang, X. Yang, Q. Ye, and X. Wu, ACS Appl. Energy Mater. 5, 8769–8780 (2022).
- ¹⁸Y. Zhai, Y. Ma, S. N. David, D. Zhao, R. Lou, G. Tan, R. Yang, and X. Yin, Science 355, 1062–1066 (2017).
- ¹⁹R. A. Yalçın, E. Blandre, K. Joulain, and J. Drévillon, ACS Photonics 7, 1312–1322 (2020).
- ²⁰A. D. Phan, V. D. Lam, and K. Wakabayashi, RSC Adv. 10, 41830–41836 (2020).
- ²¹S. Wen, X. Liu, S. Cheng, Z. Wang, S. Zhang, and C. Dang, J. Quant. Spectrosc. Radiat. Transfer 234, 1–9 (2019).
- ²²R. Incardone, T. Emig, and M. Krüger, Europhys. Lett. **106**, 41001 (2014).
- ²³M. Nikbakht, J. Appl. Phys. **116**, 094307 (2014).
- ²⁴M. Nikbakht, Europhys. Lett. **110**, 14004 (2015).
- 25 F. V. Ramirez, S. Shen, and A. J. H. McGaughey, Phys. Rev. B 96, 165427 (2017).
- 26Y. Hu, Y. Sun, Z. Zheng, J. Song, K. Shi, and X. Wu, Int. J. Heat Mass Transfer 189, 122666 (2022).
- ²⁷E. Tervo, Z. Zhang, and B. Cola, Phys. Rev. Mater. 1, 015201 (2017).
- ²⁸S. J. Petersen, S. Basu, B. Raeymaekers, and M. Francoeur, J. Quant. Spectrosc. Radiat. Transfer 129, 277–286 (2013).
- ²⁹Y. Hu, H. Li, Y. Zhang, Y. Zhu, and Y. Yang, Phys. Rev. B **102**, 125434 (2020).
- ³⁰A. Assadillayev, T. Hinamoto, M. Fujii, H. Sugimoto, and S. Raza, Nanophotonics 10, 4161–4169 (2021).
- ³¹A. W. Rodriguez, M. T. H. Reid, and S. G. Johnson, Phys. Rev. B 86, 220302(R) (2012).
- ³²A. W. Rodriguez, M. T. H. Reid, and S. G. Johnson, Phys. Rev. B 88, 054305 (2013).
- 33L. P. Walter, E. J. Tervo, and M. Francoeur, arXiv:2204.05399 (2022).
- 34S. M. Rytov, Y. A. Kravtsov, and V. I. Tatarskii, Principles of Statistical Radiophysics 3: Elements of Random Fields (Springer-Verlag, Berlin, 1989).
- 35V. Chiloyan, J. Garg, K. Esfarjani, and G. Chen, Nat. Commun. 6, 6755 (2015).

- 36 T. Tokunaga, A. Jarzembski, T. Shiga, K. Park, and M. Francoeur, Phys. Rev. B **104**, 125404 (2021).
- 37 T. Tokunaga, M. Arai, K. Kobayashi, W. Hayami, S. Suehara, T. Shiga, K. Park, and M. Francoeur, Phys. Rev. B 105, 045410 (2022).
- ³⁸C. H. Kuo, Y. C. Yang, S. Gwo, and M. H. Huang, J. Am. Chem. Soc. 133,
- ³⁹Y. J. Wang, N. Zhao, B. Fang, H. Li, X. T. Bi, and H. Wang, Chem. Rev. 115, 3433-3467 (2015).
- ⁴⁰Z. Quan and J. Fang, Nano Today 5, 390–411 (2010).
- ⁴¹K. Deng, Z. Luo, L. Tan, and Z. Quan, Chem. Soc. Rev. 49, 6002 (2020).
- ⁴²A. Martinet, C. Soler, N. Holzschuch, and F. X. Sillion, ACM Trans. Graphics
- ⁴³DGM, see https://www.mathworks.com/matlabcentral/fileexchange/58413plot-superquadratic-surfaces for "Plot Superquadratice Surfaces" (2022).
- 44 B. Czapla and A. Narayanaswamy, J. Quant. Spectrosc. Radiat. Transfer 227, 4 (2019).
- 45K. Joulain, J.-P. Mulet, F. Marquier, R. Carminati, and J.-J. Greffet, Surf. Sci. Rep. 57, 59 (2005).
- ⁴⁶S. Edalatpour and M. Francoeur, J. Quant. Spectrosc. Radiat. Transfer 133, 364 (2014). ⁴⁷A. Narayanaswamy and G. Chen, Phys. Rev. B 77, 075125 (2008).
- ⁴⁸J. Dong, J. M. Zhao, and L. H. Liu, J. Quant. Spectrosc. Radiat. Transfer 197, 114-122 (2017).
- ⁴⁹M. Luo, J. Dong, J. Zhao, L. Liu, and M. Antezza, Phys. Rev. B **99**, 134207 (2019).